Photocatalytic properties of plasma-synthesized zinc oxide and tin-doped zinc oxide (TZO) nanopowders and their applications as transparent conducting films

Arun Murali[1] [ORCID] · **Hong Yong Sohn[1]**

Abstract

Transparent conducting zinc oxide and tin-doped zinc oxide (TZO) nanopowders were synthesized for the first time using a novel plasma-assisted chemical vapor synthesis route. The injected precursors were volatized completely and rapidly followed by chemical reactions and subsequent quenching to yield fine nanopowder. The amount of tin nitrate was varied to obtain 3 and 5 at.% Sn designated as TZO1 and TZO2 respectively. XRD diffraction peaks of TZO1 nanoparticles indicated the presence of wurtzite structure without any tin oxide peaks except in TZO2 sample and SEM micrographs revealed spherical particles. The nanosized powders would make an excellent material for use as photocatalyst due to high surface to volume ratio. Optical examinations indicated that the band gap in TZO1 was redshifted to 3.16 eV from 3.22 eV in undoped ZnO nanoparticles. The photocatalytic properties of ZnO and TZO nanopowders were investigated using the methylene blue dye degradation under UV light irradiation and kinetic analyses indicated that the photodegradation of methylene blue followed pseudo-first order kinetic model using Langmuir–Hinshelwood mechanism. Furthermore, the TZO1 nanoparticles exhibited superior photocatalytic activity compared with ZnO and the improvement was ascribed to increase in specific surface area and enhanced oxygen vacancies as revealed from the XPS O 1s and PL spectra. Deposited films showed a hexagonal wurtzite structure and exhibited a c-axis preferred orientation perpendicular to the substrate. A minimum resistivity of 1.4×10^{-3} Ωcm was obtained at lower doping amount of 3 at.% Sn as in TZO1 film and all the films exhibited an average transmission of 80% indicating their suitability as a promising material in optoelectronic applications. Optical constants of the films were determined, which varied with doping amount. The photo-current properties of ZnO and TZO films were investigated and only TZO1 film showed photo response property when irradiated with UV lamp.

1 Introduction

Transparent conducting oxides (TCO) are of great scientific and commercial importance because of its high optical transparency in the visible region and excellent conductivity. TCO's are commonly used in transparent transistors, gas-sensing devices, light emitting diodes and electro-optical devices [1].

Zinc oxide (ZnO) is a II–VI group compound semiconductor which crystallizes in wurtzite structure belongs to the space group P6$_3$mc and has properties of high optical transparency, non-toxicity, good UV trapping, etc. which are

an essential properties of optoelectronic due to its large band gap of 3.37 eV and exciton binding energy of 60 meV [2, 3]. However, ZnO films, have poor conductivity and doping with various dopants are usually necessary to improve the conductivity for as use as TCO film. Replacing Zn^{2+} ions with higher valence ions such as Al^{3+} and Sn^{4+} ions brings about significant changes in electrical and optical properties [4, 5]. At present, indium tin oxide (ITO) is the most commonly used TCO's, but due to concerns of the supply of world indium reserves and cost of indium, there has been an increasing interest in alternatives [6].

Tin-doped zinc oxide (TZO) is an important alternative to ITO and is widely used as transparent electrode in various kind of devices. When Sn was added into ZnO for doping, Sn^{4+} substitutes Zn^{2+} sites in the ZnO crystal structure because of its smaller ionic radius (0.069 nm) than Zn^{2+} (0.074 nm) which results in the addition of two more free electrons and thereby improving the electrical conductivity [7]. The electrical

✉ Arun Murali
arun.murali@utah.edu

1   Department of Metallurgical Engineering, University of Utah, Salt Lake City, UT, USA

conductivity, transparency, thermal stability, and durability make this material interesting and attractive [8, 9].

Dyes are important source of environmental pollution and it is used in many industrial processes, namely cosmetic, textile, and printing [10]. Nearly 15% of the world production of dyes, lost during the process of dying is released as textile effluents [10]. Methylene Blue which is a cationic dye is primarily used in the textile industry and the discharge of large amounts of effluent is harmful to microbes, aquatic system and human health [11]. The effects of colored water is detrimental to environment since its color blocks the sunlight access to aquatic organism and plants, which in turn diminishes photosynthesis and affects the ecosystem [12]. In recent years, an advanced oxidation process utilizing photocatalyst has gained a significant deal of importance in wastewater treatment because of its low consumption of energy, mild reaction condition and high activity compared to other reported methods [13, 14].

Photocatalytic degradation mechanism is explained as follows. When the photocatalyst is irradiated with photons having energy either equal to or more than the photocatalyst's band gap, then the electrons from the valence band get excited to its conduction band, leaving behind holes in the valence band [15, 16].

$$Photocatalyst + hv \rightarrow e_{CB}^- + h_{VB}^+ \qquad (1)$$
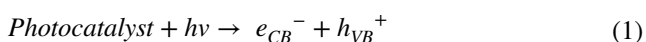
The electrons are trapped by the dissolved O_2 or by the adsorbed O_2 to give rise to superoxide radicals:

$$e_{CB}^- + O_2 \rightarrow O_2^{\cdot-} \qquad (2)$$

The superoxide radicals react with H_2O_2 to form hydroperoxyl radicals ($HO_2^{\cdot}$) and hydroxyl radicals ($OH^{\cdot}$) which are considered strong oxidizing agents that decomposes the organic molecules.

$$O_2^{\cdot-} + H_2O \rightarrow HO_2^{\cdot} + OH^{\cdot} \qquad (3)$$

The photoinduced holes trap hydroxyl groups on the surface of the photocatalyst to give rise to hydroxyl radicals:

$$h_{VB}^+ + OH^- \rightarrow {}^{\cdot}OH_{ads} \qquad (4)$$

$$h_{VB}^+ + H_2O \rightarrow {}^{\cdot}OH + H^+ \qquad (5)$$

Thereby organic molecules will get oxidized to yield CO_2 and H_2O as follows:

$${}^{\cdot}OH + organic\ molecules + O_2 \rightarrow products\ (CO_2 + H_2O) \qquad (6)$$
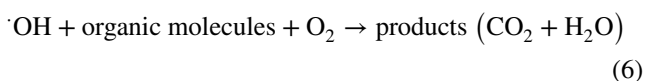
Meanwhile, the recombination of positive hole and electron will take place which reduces the photocatalytic activity of prepared TZO photocatalyst.

$$e_{CB}^- + h_{VB}^+ \rightarrow Photocatalyst \qquad (7)$$

For the first time, a novel plasma- assisted chemical vapor synthesis technique has been used for the preparation of tin-doped zinc oxide (TZO) nanopowder. Thermal plasma offers

a high processing rate and advantages like achieving a good control of size, shape and crystal structure is also possible [17]. It offers availability of high processing temperature to vaporize the precursors completely and rapidly and the temperature is high enough to decompose the injected reactants into atoms and radicals, which then react and condense to form nanosized particles by rapid quenching when cooled by either mixing with cool gas or expansion through the nozzle [17]. Since the synthesis technique is performed in a clean reaction atmosphere, high purity products are produced. Rapid quenching in the cooling chamber allows for the formation of nano-sized products and a broad choice of precursors can be selected for injection in plasma torch [18]. Plasma- assisted vapor synthesis is a single stage process and avoids multiple steps which are involved in mechanical milling, precipitation and sol–gel method. There is no requirement of high volume of liquids and surfactants, that are essential prerequisites for any wet-chemical processes [18]. Unlike other gas-phase methods, synthesis is carried out in gas-phase at atmospheric pressure without necessitating the need of expensive vacuum system. Synthesis can also be carried out in continuous process and has a high potential for large-scale production in many industrial applications [19].

Preparation of thin films of transparent conducting oxides (TCO) have been carried out by large sorts of deposition techniques mainly physical and chemical techniques. All these techniques are time-consuming process and costly [18]. Over other techniques, fabricating films from well dispersed nanoparticles is a good replacement. In addition to cost-effective technique, through this technique a good control of composition ratio and synthesized nanoparticles can be used effectively to reduce the loss of materials [20, 21]. Different synthesis techniques of TZO nanoparticles have been reported. Wu et al. [22] fabricated Sn-doped ZnO nanorods by hydrothermal treatment and used methyl orange as the probe molecule to evaluate its photocatalytic activity. Wang et al. [23] prepared tin-doped zinc oxide nanoparticles in organic solution, with metal acetylacetonate as the precursor and oleyl amine as the solvent. Javid et al. [24] synthesized TZO nanoparticles by chemical solution method using zinc nitrate and NaOH as precursors. Junlabhut et al. [25] synthesized TZO nanopowders by co-precipitation method with various Sn additives from 0 to 50 wt%. Verma et al. [26] reported the structure–property relationship in undoped and Sn-doped ZnO nanostructured materials synthesized by co-precipitation. Li et al. [27] used the substrate of p-type Si (100) for synthesizing TZO nanowires involving a vapor-liquid-solid growth process. In this study, zinc oxide and tin-doped zinc oxide nanopowders were synthesized by the plasma process and tested for its photocatalytic property in the degradation of methylene blue. The obtained nanopowders were also used to fabricate ZnO and TZO films to

investigate the influence of Sn doping on their structural, optical, electrical and photocurrent properties. The high figure of merit and obtained resistivity values were much lower than that of reported results on TZO films [28–30], indicating their suitability for use as transparent electrical contacts in optoelectronic devices.

2 Experimental apparatus

The plasma-reactor system used in this work consisted of following components: (a) plasma torch having a copper cathode and tungsten anode (b) power supply unit (c) cylindrical reactor made of water-cooled stainless-steel tube (d) cooling system (e) powder feeding and delivery system (f) powder collector system (g) primary gas and carrier gas delivery system and (h) off-gas scrubber and exhaust system, as shown in Fig. 1. Details about the experimental set-up are to be found in our previous publications [18, 31].

3 Experimental procedure

The precursors used for synthesizing zinc oxide and tin-doped zinc oxide in this work were as follows: (1) zinc nitrate [$Zn(NO_3)_2 \cdot 6H_2O$, Alfa Aesar, Haverhill, MA] powder for zinc oxide, and (2) a mixture of zinc nitrate [$Zn(NO_3)_2 \cdot 6H_2O$, Alfa Aesar, Haverhill, MA] and tin nitrate [$Sn(NO_3)_4$, American Elements, Los Angeles, CA] powders for tin-doped zinc oxide. Precursors were crushed and sieved to obtain a final particle size of ~ 50 μm. The sieved precursors were dried at 50 °C for removing moisture so as to

permit an easy flow of powders through the powder feeding tube. Vibrating mixer was used to thoroughly mix the precursors and was then injected into the plasma flame torch using the above stated power feeding system.

Experimental conditions used were as follows: (1) flow rate of plasma gas (Ar): 40 l/min (25 °C and 86.1 kPa total pressure at Salt Lake City); (2) feeding rate of precursor: 0.5 g/min; (3) carrier gas flow rate (Ar): 3.5 l/min; (4) plasma power was set at 15 kW. Amount of tin nitrate was altered to achieve 3 and 5 at.% Sn designated as TZO1 and TZO2 respectively.

3.1 Analysis methods for nanoparticles

The produced nanoparticles were characterized by X-ray diffraction technique (Rigaku D/Max-2200V) for structural analysis, Scanning Electron Microscope (Hitachi S-4800) equipped with an Energy Dispersive Spectrophotometer (EDS) system for analysis of surface morphology, X-ray photoelectron spectroscopy (Kratos Axis Ultra DLD) for analyzing the chemical state of Zn, Sn and O in ZnO and TZO nanopowders. Micro Raman spectrometer (WITec Alpha SNOM) using a He-Ne laser as the excitation source was used for Raman analysis. The absorption spectra of ZnO and TZO with various dopant concentrations were analyzed by diffuse reflectance spectroscopy (DRS) in which the scanning was done in the 300–800 nm wavelength range. Perkin Elmer spectrophotometer with a Xe lamp using an excitation wavelength of 350 nm was used to examine the Photoluminescence (PL) spectra.

3.2 Photocatalysis set-up

Photocatalytic degradation of methylene blue by ZnO and TZO with various doping concentrations was carried out in 1-l volume reaction vessel, as shown by a schematic sketch in Fig. 2. The reaction vessel is fabricated of borosilicate glass to house the immersion well. The quartz immersion well is double-walled and consisted of an inner diameter tube through which cooling water was flown. Cooling water was circulated to control the solution temperature. 450 W mercury vapor lamp was inserted vertically in the immersion well. Approximately 60% of the radiated energy is in the ultraviolent portion of the spectrum, 35% in the visible region and the balance in the infrared range. A 6-foot power cord allowed for lowering lamp into the well. Flat bottom of the reactor allows the use of a magnetic stirrer. The volume in the reactive area of lamp was 45% of the total volume. The reaction vessel had a 14/20 size taper joint for withdrawing the solution after certain time intervals using sparger tubes and one side arm provision for thermometer insertion. The transformer operating at 115 V and 60 Hz was used for supplying extra voltage and current needed for initiation of arc.
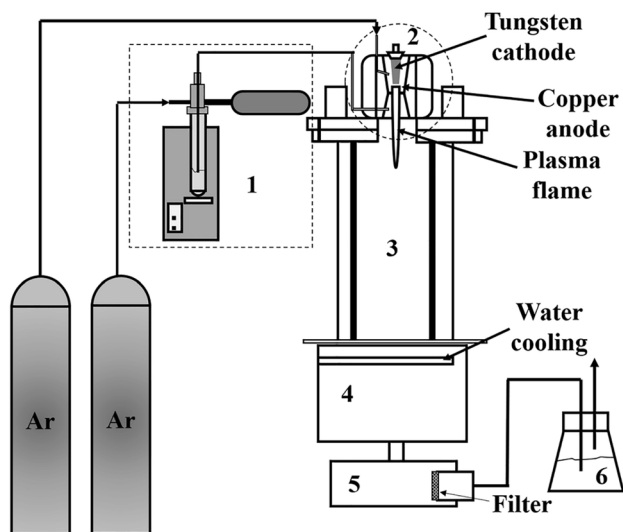

Fig. 1 Plasma reactor system consist of : (1) powder feeding system, (2) plasma gun, (3) reactor chamber, (4) cooling chamber, (5) powder collector, and (6) scrubber
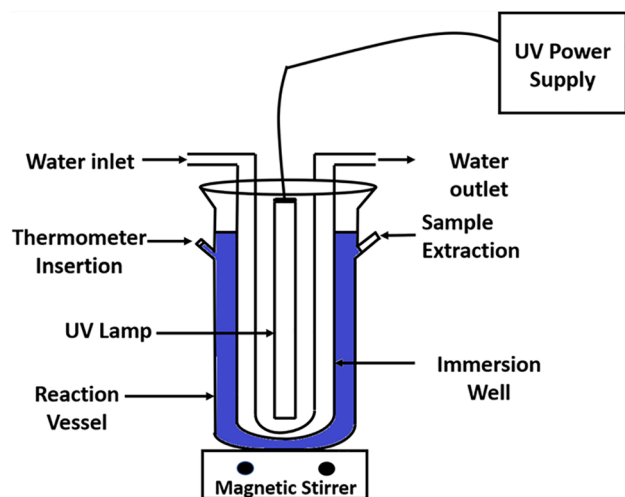
Fig. 2 Schematic diagram of the experimental set-up used for photocatalysis tests

3.3 Measurement of photocatalytic activity

Photocatalytic activity of the prepared slurry was evaluated by the degradation of a methylene blue solution. Before the illumination of UV light, the slurry was magnetically stirred for 30 min to achieve an equilibrium of adsorption and desorption. The slurry was prepared with 0.1 g of the photocatalyst dispersed in 500 ml of 85 μM methylene blue (MB) solution. At time intervals of 20 min, 10 ml of the solution were collected from the slurry suspension and centrifuged at 5000 rpm for 10 min. The centrifuged MB solution was filtered to remove any particle. The filtrate was then analyzed by using a UV–Vis spectrophotometer (Shimadzu UV-3600) by measuring the light absorption intensity at 664 nm where the maximum absorption intensity was attained. A calibration plot was prepared that relates absorbance to the concentration of methylene blue based on Beer–Lambert's law. The reaction kinetics of the photocatalysis in general obeys the following Langmuir–Hinshelwood (L–H) equation [32]:

$$R = \frac{dC}{dt} = -\frac{k_s K C}{(1 + KC)} \tag{8}$$

where k_s is the surface reaction rate constant, K is the adsorption coefficient of the reactant, and C is the concentration of methylene blue at time t. However, when concentrations of methylene blue is low and due to weak adsorption ($KC \ll 1$), Eq. (8) is simplified to

$$R = \frac{dC}{dt} = -kt \tag{9}$$

where $k = K k_s$.

Integration of Eq. (9) gives:

$$Ln(C) = -kt + Ln(C_0) \tag{10}$$

where C_0 is the initial concentration of methylene blue, k is the pseudo-first-order reaction rate constant (min^{-1}), and t is the reaction time (min). The reaction rate constant (k) was calculated from the slope of ln(C) versus time plot. The % degradation was determined using the following formula:

$$\% \text{ degradation} = \frac{C_i - C_f}{C_i} \times 100 \tag{11}$$

where C_i and C_f are the initial and final concentrations of the dye.

3.4 Preparation of thin films

ZnO and TZO nanopowders with different dopant concentrations were mechanically dispersed in polyethylene glycol (PEG$_{600}$) and carbonic acid was added as a dispersion agent. The wetted powder was then ground in mortar to obtain a homogenous paste. The paste was then dissolved in 1-propanol. ZnO and TZO coatings were prepared by the spin coating process on a 2.5 cm square-shaped borosilicate glass substrate using the dispersion at 2000 rev/min for nearly 1 min. Coatings were densified to a temperature of 500 °C in an Ar atmosphere.

3.5 Analysis method for thin films

ZnO and TZO films were then analyzed using a X-ray diffractometer with Cu Kα radiation ($\lambda = 1.5406$ Å) from 10.00° to 80.00° at a scanning speed of 0.02°/s. 4-probe technique was used to measure the sheet resistance and Hall effect measurements were also performed to measure the carrier density and mobility of deposited films using the same technique under applied magnetic field of 0.35 T. The optical properties were measured using an UV-Vis-NIR spectrophotometer.

4 Results and discussions

4.1 X-ray diffraction (XRD)

The XRD patterns of ZnO, TZO1 and TZO2 are shown in Fig. 3. The peaks were indexed using the X'Pert High Score Plus, and the peaks correspond to the hexagonal wurtzite structure of ZnO. Narrow and sharp peaks confirm the good crystallinity of synthesized nanopowder. No SnO$_2$ or other Sn phases were detected in TZO1 sample but in TZO2 sample, SnO$_2$ phase was observed indicating that the Sn content has exceed its maximum solubility in ZnO. The presence of
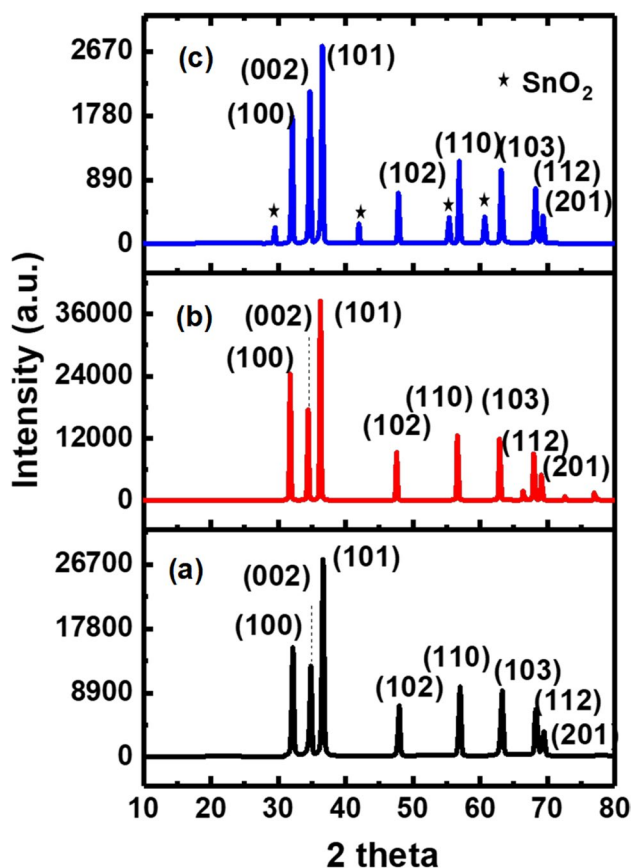
Fig. 3 XRD diffraction patterns of **a** ZnO, **b** TZO1 and **c** TZO2. All the peaks correspond to the hexagonal wurtzite structure of ZnO. SnO_2 peaks are observed in TZO2 sample

Table 1 Crystallite size calculated from XRD analysis

Type	Size (100) nm	Size (002) nm	Size (101) nm	Average crystallite size (nm)	Average lattice constant 'a' (Å)
ZnO	56.3	59.4	56.2	57.3	3.28
TZO1	21.4	24.7	20.2	22.1	3.27
TZO2	38.5	38.4	38.3	38.4	3.27

the full width at half maximum and β_0 is the correction factor (0.005 rad).

The crystallite size is determined from the three peaks (100), (002) and (101) and the average size is calculated. The lattice constants are calculated by the following equation [34, 35]

$$\frac{1}{d(hkl)^2} = \frac{4}{3}\left(\frac{h^2 + hk + k^2}{a^2}\right) + \frac{l^2}{c^2} \tag{13}$$

where *a, c* are the lattice constants and *d (hkl)* is the crystalline plane distance for indices (hkl) calculated from the XRD pattern. The position of the most intense peaks are slightly shifted towards a higher angle as compared to the ZnO XRD pattern which confirms the replacement of Zn^{2+} by Sn^{4+} ions at its substitutional sites [7]. The crystallite size is decreased on increasing the doping amount to 3 at.% as in TZO1 and a simultaneous decrease in FWHM is also observed as shown in Table 1.

4.2 Raman spectroscopy

ZnO has a wurtzite structure and the symmetry of the ZnO crystal structure lies in the spatial group of C_{6v}^4 with two formula units in the primate cell. Therefore, its optical properties at the center of Brillouin zone (Γ^-) is represented by the following irreducible relation [36]:

$$\Gamma^- = 1A_1 + 2B_1 + 1E_1 + 2E_2 \tag{14}$$

The polar characteristics of A_1 and E_1 modes are split into LO (longitudinal) and TO (Transverse) modes, with different frequencies. Modes A_1, E_1 and E_2 are Raman and infrared active whereas the two B_1 modes are infrared and Raman inactive and are silent modes [36, 37]. A single broad LO peak is observed at 588 cm^{-1} which is due to the overlapping of $A_1(LO)$ and $E_1(LO)$ modes. In this study, as shown in Fig. 4, a strong and a sharp peak at 437 cm^{-1} is attributed to the high frequency of E_2(high) mode and is the characteristic feature of hexagonal wurtzite structure of ZnO [38]. ZnO & TZO1 exhibited high intense Raman peaks suggesting improved crystal quality whereas for TZO2, the intensity of E_2(high) mode decreased indicating that the crystallinity of TZO2 nanopowder gets deteriorated at a higher doping

SnO_2 phase as observed in TZO2 lowers the crystallinity of TZO nanopowder which is evident from the decrease in the intensity of peaks. Small shifts in the diffraction peaks are observed in TZO1 and TZO2 to higher diffraction angles with the doping of tin into the zinc oxide lattice. Crystallite size is decreased with Sn concentration at 3 at.% (TZO1), which is due to lattice shrinkage from the variations in the ionic radii of Zn^{2+} and Sn^{4+} ions a mentioned above. However, an increase in the crystallite size is observed in TZO2 (5 at.%), which is due to an excess segregation of Sn^{4+} ions to its grain boundaries. The reflections (100), (002) and (101) are of high intensity and other reflections (102), (110), (103) and (112) are of lower intensity. Since the (101) reflection is the highest in all the samples, we can conclude the particles are orientated mostly in the [101] direction. In TZO2, excess Sn^{4+} serves as an inhibitor for the growth of particles in the [101] direction. The crystallite size was calculated from Debye–Scherrer equation [33]:

$$D = K\lambda/(\beta \cos\theta) \tag{12}$$

where $\beta = \sqrt{(\beta^2_{(FWHM)} - \beta^2_0)}$ is the peak broadening after subtracting the instrumental broadening effect, $\beta_{(FWHM)}$ is
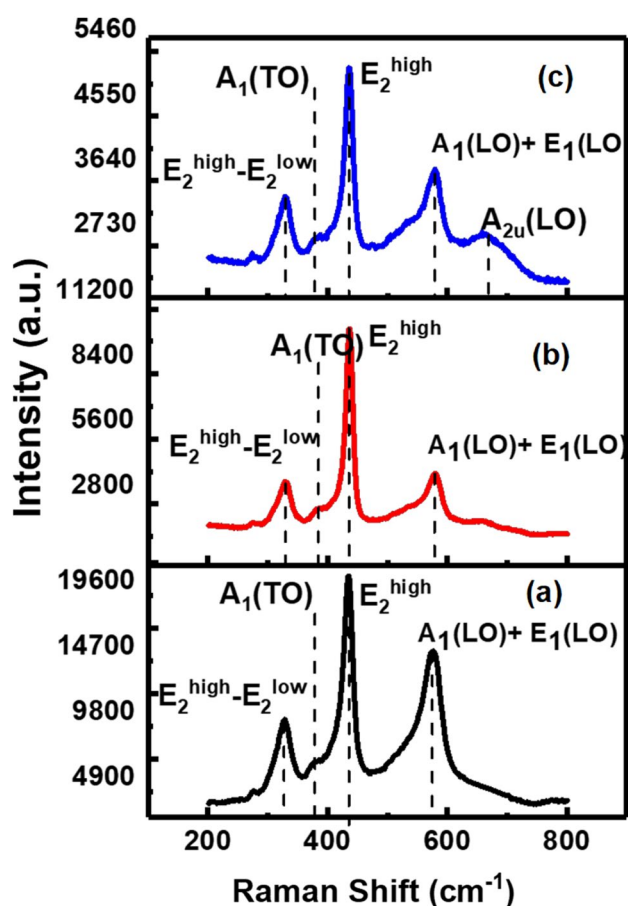
Fig. 4 Raman spectra of **a** ZnO, **b** TZO1 and **c** TZO2. Decrease in the intensity of E_2 (high) mode in TZO2 sample indicates the decrease in the crystal quality at higher doping amount of 5 at.% Sn

amount and this observation corroborates with the XRD data. Junlabhut et al. [25] also reported that the Raman signals obtained in TZO nanopowders are highly sensitive to crystalline nature. A small peak shift was observed in the E_2(high) mode for TZO2 sample with the usual position of ZnO at 437 cm^{-1}, indicating the decreased order of wurtzite phase after the introduction of Sn^{4+} ions in the ZnO crystal lattice. The peak at 670 cm^{-1} corresponding to A_1 mode appears only in TZO1 and TZO2 [25, 39]. The intensity of this peak is significantly stronger in TZO2 than in other samples.

### 4.3 X-ray photoelectron spectroscopy (XPS) and photoluminescence spectroscopy (PL)

XPS analysis was performed to ascertain the concentration of Sn and to ascertain the valence of Sn in TZO1 and TZO2. The difference in binding energy of 23.10 eV between Zn 2p$_{3/2}$ and Zn 2p$_{1/2}$ and the binding energy position indicates that Zn in ZnO, TZO1 and TZO2 nanopowder exist in 2+ oxidized state. To ascertain the valence state of Sn, Sn 3d spectra was

also obtained from the samples under study. The Sn 3d$_{5/2}$ and Sn 3d$_{3/2}$ peaks are located at 486.6 and 495.2 eV, respectively. The obtained Sn 3d$_{3/2}$ signal was intense due to the Auger ZnL$_3$M$_{45}$M$_{45}$ transition [40], as a result it was difficult for comparing the spectral parameters of Sn 3d$_{3/2}$ with those of the reference standard exactly. Binding energy position of Sn 3d$_{5/2}$ at 486.6 eV indicated that Sn is incorporated in the form of Sn^{4+} state [41–43]. This further gives support to the Sn^{4+} ions substituting for Zn^{2+} sites. The observed Sn 3d$_{5/2}$ peak also ruled out the possibility of segregation of metallic Sn and the presence of other phases like SnO. Zn 2p spectra are located at 1021.42 and 1044.34 eV, as shown in Fig. 5a, which corresponds to Zn 2p$_{3/2}$ and Zn 2p$_{1/2}$, respectively. Intensity of Sn 3d$_{5/2}$ increased with doping amount of Sn as shown in Fig. 5b. XPS results showed an asymmetric shape of O 1s spectra as shown in Fig. 6. Gaussian fitting method was adopted to deconvolute O 1s peak into three components. The peak located at 529.92 eV refers to O^{2-} species in the wurtzite structure of ZnO. At higher binding energy in O 1s spectra, contributions from oxygen vacancies and chemisorbed oxygen species are observed. The intermediate binding energy peak (531.4 eV) and the higher binding energy peak (532.4 eV) are connected with oxygen vacancies and chemisorbed oxygen species respectively [19, 44–46]. The changes in the intensity of O_v component is in connection with the variation in the oxygen vacancies concentration [47, 48]. It was observed in our study that with Sn addition, a relative increase in intensity of component O_v to O_L^{2-} component was observed, which confirmed that the concentration of oxygen vacancies varies with doping amount. The PL spectra of undoped and Sn-doped ZnO nanopowders are shown in Fig. 7. All of the spectra showed a strong UV emission peak and a green emission peak (deep-level emission) in the visible region. The UV emission also known as near-band edge emission arises from the band edge recombination of free excitations [49] and green band emission peak is related to the singly ionized oxygen vacancies in ZnO, and this peak originates from the recombination of a photo generated hole with singly ionized charge state of this defect [49, 50]. It is evident that the ratio of DLE/UV is larger for TZO1 followed by TZO2 and ZnO nanopowders. Thus, the weak green band edge emission in the PL spectrum for undoped ZnO indicates low concentration of oxygen vacancies present. This further confirms that in TZO, Sn atoms exist at substitutional sites and share the oxygen with Zn atoms and hence increases the concentration of oxygen vacancies enhances the intensity of green band emission.

4.4 Scanning electron microscopy–energy dispersive spectroscopy (SEM–EDS)

SEM micrographs of TZO1 particles are show in Fig. 8a. Spherical shaped morphology with no agglomeration was seen for all compositions of ZnO and TZO particles.

Fig. 5 **a** XPS Zn 2p core level spectra of TZO1 and TZO2. The binding energy difference of 23.10 eV between Zn $2p_{3/2}$ and Zn $2p_{1/2}$ and binding energy positions indicates that Zn in TZO nano powder exist in 2+ oxidization state. **b** XPS Sn 3d spectra of TZO1 and TZO2. The binding energy of 486.6 eV indicates that Sn is incorporated in the form of Sn^{4+} bonding state from SnO_2 and the intensity of Sn 3d spectra increases with an increase in doping amount
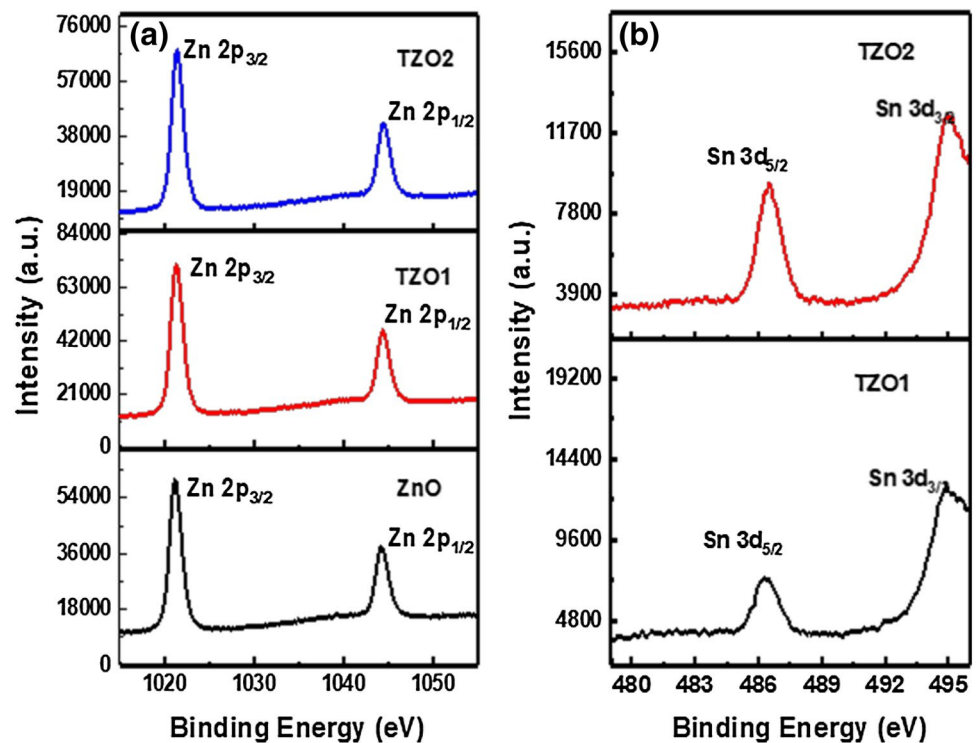
Morphologies like nanorods [22], cubic like structures [25], nanowires [27] have been reported for TZO nanoparticles. EDS spectrum for TZO1 nanoparticles is shown in Fig. 8b. Appearance of Zn $L\alpha_1$ and Sn $L\alpha_1$ peaks at 1.1 and 2.7 keV confirmed the presence of zinc and tin elements respectively. EDS results also confirmed that the elemental distribution of zinc and tin is uniform and the Sn/Zn (at.%) composition in the nanoparticles nearly matches with designed compositions.

4.5 Photocatalysis data and absorption spectrum analysis

The photocatalytic activity of ZnO, TZO1 and TZO2 nanopowders were investigated using MB as an indicator under UV light. The results demonstrated that TZO1 is a superior photocatalyst to ZnO. From Fig. 9, it is clear that the degradation of MB is enhanced significantly when catalyzed by Sn-doped ZnO nanopowder. The percentage degradation increased from 42.0 to 94.6%. The degradation rate constant for TZO1 increased to 0.0339 min^{-1} from 0.0106 min^{-1} as shown in Fig. 10a. The enhanced photocatalytic efficiency of TZO1 is attributed to an enhancement in the specific surface area and also due to the band gap of the nanopowder. Upon doping Sn in ZnO, the BET specific surface area increased from 18.5 to 48.6 m^2/g. The enhanced S/V ratio facilitated an increase in the number of the active states on the photocatalyst surface and thereby increased the concentration of photo generated carriers [51]. Thus, the

relative number of free radicals attacking the dye molecules increases. Another factor influencing the rate of degradation is the band gap. Figure 10b shows TZO1 nanoparticles have maximum absorbance at 395 nm that corresponds to a band gap of 3.16 eV which was redshifted compared to undoped ZnO nanoparticles. ZnO showed a maximum absorbance at 383 nm corresponding to a band gap of 3.22 eV and thereby indicating that TZO nanoparticles have higher absorption that is TZO nanoparticles have photocatalytic activity higher than ZnO nanoparticles. The red shift observed with lower band energy was also observed for other doped ZnO samples. Ravishankar et al. [52] reported that the band gap of Ag-doped ZnO nanoparticles was red-shifted compared to that of undoped ZnO sample. Rajbongshi et al. [53] reported a red shift in N-doped ZnO compared to that of pristine ZnO. When doped ZnO gets excited by photons with energy greater than or equal its bandgap energy, a larger number of free electrons are excited from VB to CB of ZnO and SnO_2, leading to generation of electron–hole pairs. The transfer of electrons from the CB of ZnO to CB of SnO_2 and conversely, the holes transfer from the CB of SnO_2 to CB of ZnO decreases the recombination rate of charge carriers [54]. This way, by separating the arrival time of electrons and holes at the surface of the photocatalyst, the probability of recombination of photogenerated charge carriers is restrained, facilitating an enhancement in photocatalytic activity at lower doping amount of Sn as in TZO1. Higher photocatalytic activity in TZO1 is also attributed to higher oxygen vacancies, revealed from the PL spectra. Oxygen
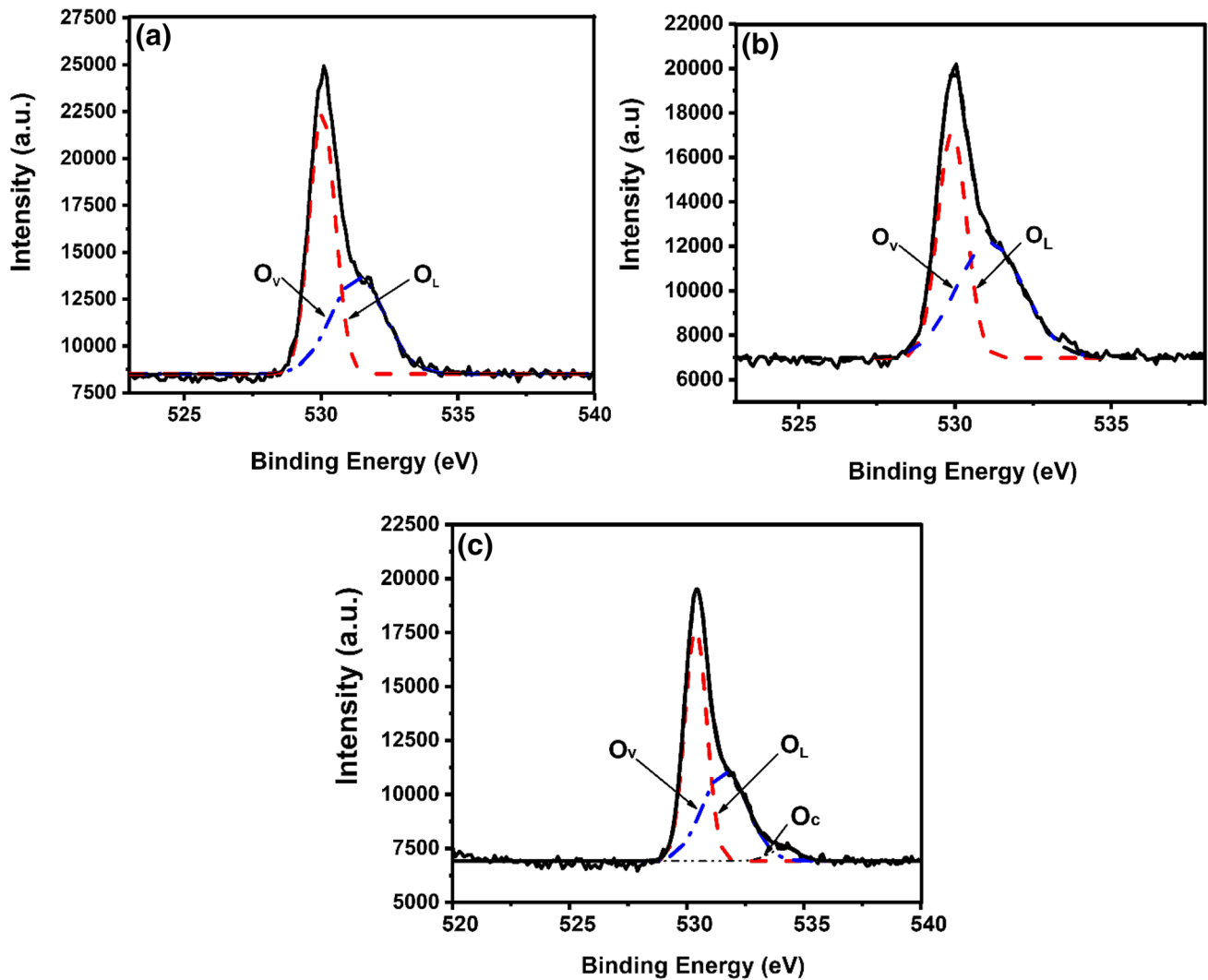
Fig. 6 XPS O1s spectra for **a** ZnO, **b** TZO1 and **c** TZO2. The oxygen peak was deconvoluted into three components with different binding energies. A relative increase in intensity of component O_v to O_L^{2-} component indicates that the concentration of oxygen vacancies varies with Sn addition

vacancy is an important reason for band gap narrowing, as observed above in conjunction with Fig. 7. Ansari et al. [55] reported the formation of band tail below the CB of ZnO caused by O-vacancy level energies and Wang et al. [56] reported the creation of impurity level by O-vacancy level energies nearer to the VB than tin undoped ZnO nanopowder. Oxygen vacancies facilitate a reduction in the recombination rate of electrons and holes. These vacancies act as electron acceptors during the photocatalytic reaction, thereby ensuring that holes in the valence band react with the hydroxyl ions to produce hydroxyl radicals, which are the main oxidant species [55–57]. Wu et al. [22] reported that the photocatalytic activity of Sn-doped ZnO catalyst increased with an increase in Sn content. In this range of Sn contents, peaks corresponding to SnO_2 crystal or other Sn phases were not detected. They concluded that an increase in

the catalytic activity with Sn content within their range was because of an increase in the singly ionized oxygen vacancy.

To study the optimum Sn doping amount, the photocatalytic activity of TZO2 nanopowder was investigated in the present work. It was apparent that the photocatalytic activity of TZO2 was lower than that of TZO1. This is due to the fact that at higher doping concentrations, the excess Sn cannot enter the lattice of ZnO crystal or further alter the bandgap and segregates at grain boundaries to form defect clusters. These defect clusters serve as recombination centers and against the separation of excited electron and hole [58]. The ratio of the intensities of DLE to UV emission peaks obtained was lower for TZO2 (5 at.% Sn) sample than for TZO1 (3 at.% Sn) indicating a decrease in the oxygen vacancies concentration and corresponding decline in the photocatalytic activity of TZO2 sample was observed.
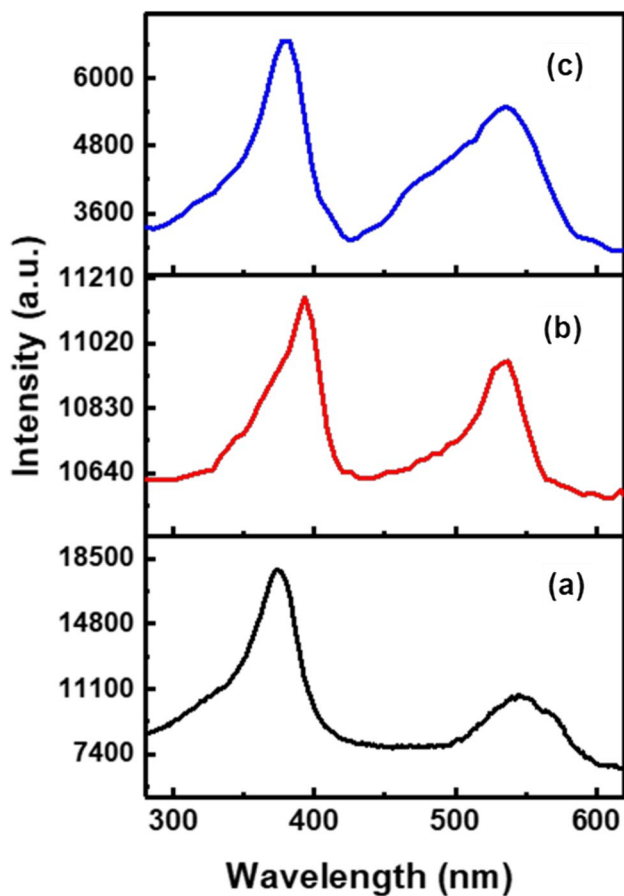
Fig. 7 PL spectra for **a** ZnO, **b** TZO1 and **c** TZO2. Oxygen vacancies enhance the intensity of green band emission and the ratio of DLE to UV is larger for TZO1 sample followed by TZO2 and ZnO samples

Fig. 8 **a** SEM micrographs of TZO1 particles synthesized at 10 kW and **b** EDS spectrum for TZO1 sample synthesized at 10 kW. Spherical shaped morphology with no cluster formation observed for all the compositions of TZO and for ZnO samples

4.6 Thin films analysis

4.6.1 X-ray diffraction (XRD)

The crystalline quality and orientation of the ZnO and TZO thin films prepared in this work were investigated by means of XRD. All the films exhibited a sharp peak near 34.54° corresponding to the (002) plane of the hexagonal wurtzite structure of ZnO and exhibited a *c*-axis orientation perpendicular to the substrate surface [59], which is evident from the sharp and strong (002) diffraction peak as shown in Fig. 11. It is clear that with the addition of Sn content, the crystalline quality of the TZO1 thin film remained the same as the ZnO film. In TZO1, the (002) plane becomes sharper and narrower as compared to the TZO2 film. The decrease in intensity at the (002) plane for the TZO2 film and increase in the intensity of (101) and (004) indicated that excess Sn deteriorates the crystalline quality of thin film due to lattice distortion. Bedia et al. [29] also reported the variations in the intensity of (002) plane with Sn content and indicated that the quality of film was improved with 1% Sn concentration.
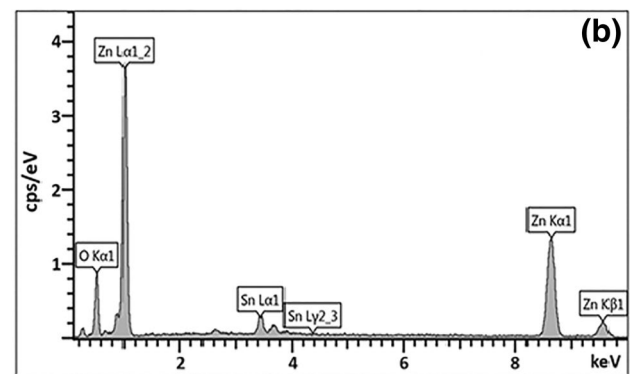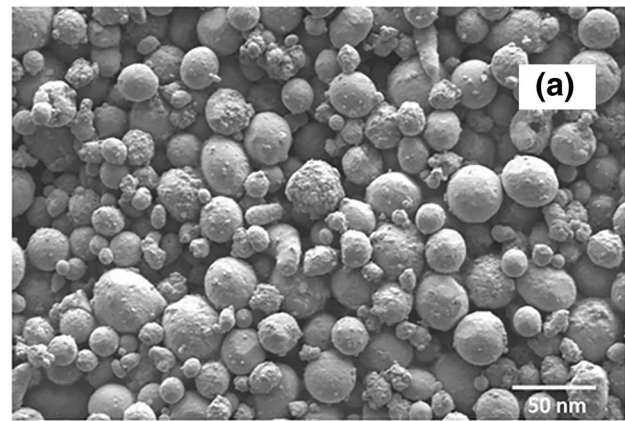
The lattice distortion is due to segregation of excess Sn to its non-crystalline regions that act as centers of scattering and thereby reduces the orientation of c-axis [60, 61].

4.6.2 Electrical properties

Room temperature electrical properties of the thin films were recorded using the four-probe technique. Current vs voltage curve showed a linear relationship, which demonstrated the ohmic nature of undoped and doped films, as shown in Fig. 12. The resistivity of TZO1 decreased from 8.2×10^{-3} Ωcm to 1.4×10^{-3} as compared to that of the undoped ZnO thin film. The decrease in the resistivity of TZO1 is due to the increase in the crystallinity of the thin film, which is in good agreement with that of the XRD results as discussed above and also due to the replacement of divalent Zn^{2+} with the tetravalent Sn^{4+} ions, hence more free electrons are generated for its electrical conduction. No decrease in the resistivity was observed at higher doping amount of 5 at.% Sn that is in TZO2 film. In TZO2 film, increase in resistivity was observed
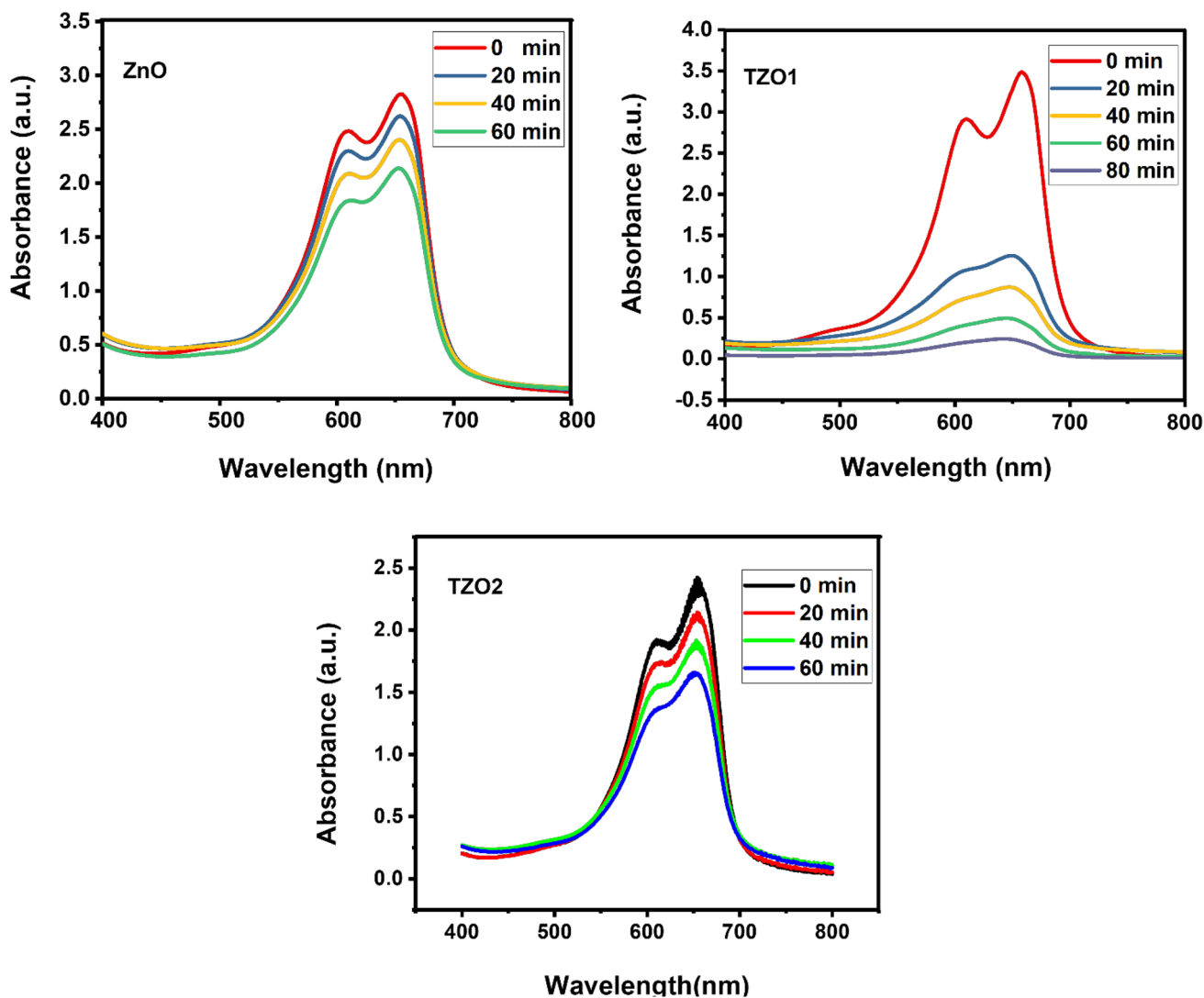
Fig. 9 Absorption spectra of methylene blue at different intervals of time using photocatalyst: ZnO, TZO1 and TZO2. The degradation of methylene blue is enhanced significantly when TZO1 sample was used as catalyst

which is attributed to the segregation of excess Sn dopant at grain boundaries which act as carrier traps [62]. Shelke et al. [28] observed a similar decrease in resistivity with the incorporation of Sn dopants compared to undoped ZnO film and an increase in the resistivity at higher doping concentration. The minimum resistivity reported by them was 3.11 Ωcm noted for 4 at.% Sn. Nasir et al. [30] reported a minimum resistivity of 3.08×10^3 Ωcm at 4 at.% Sn and Bedia et al. [29] observed a minimum resistivity of 2.1×10^{-2} Ωcm at 1 at.% Sn. The reported minimum resistivity values were much higher than our current study. Hall measurement derived electrical properties of films is shown in Table 2 and it is evident that the mobility reached maximum value in TZO1 for which the resistivity was calculated to have a minimum value.

4.6.3 Optical properties

The optical properties of the thin films were determined in the wavelength range of 300–800 nm. Transmission spectra of synthesized films is shown in Fig. 13. The transmission spectra of all the films exhibited an average transmission of 80%. The absorption edge slightly is shifted to a higher wavelength in the TZO1 film compared with the ZnO film. All films exhibited a ripple pattern, which revealed a homogeneous surface and good adhesion on glass substrates. Similar results were obtained for films deposited on glass substrates by spray pyrolysis [29]. Shelke et al. [28] also observed a similar oscillating nature in TZO films with an optical transmittance above 85% in visible region and a decrease in transmittance at higher doping concentration. Refractive index and extinction coefficient are important
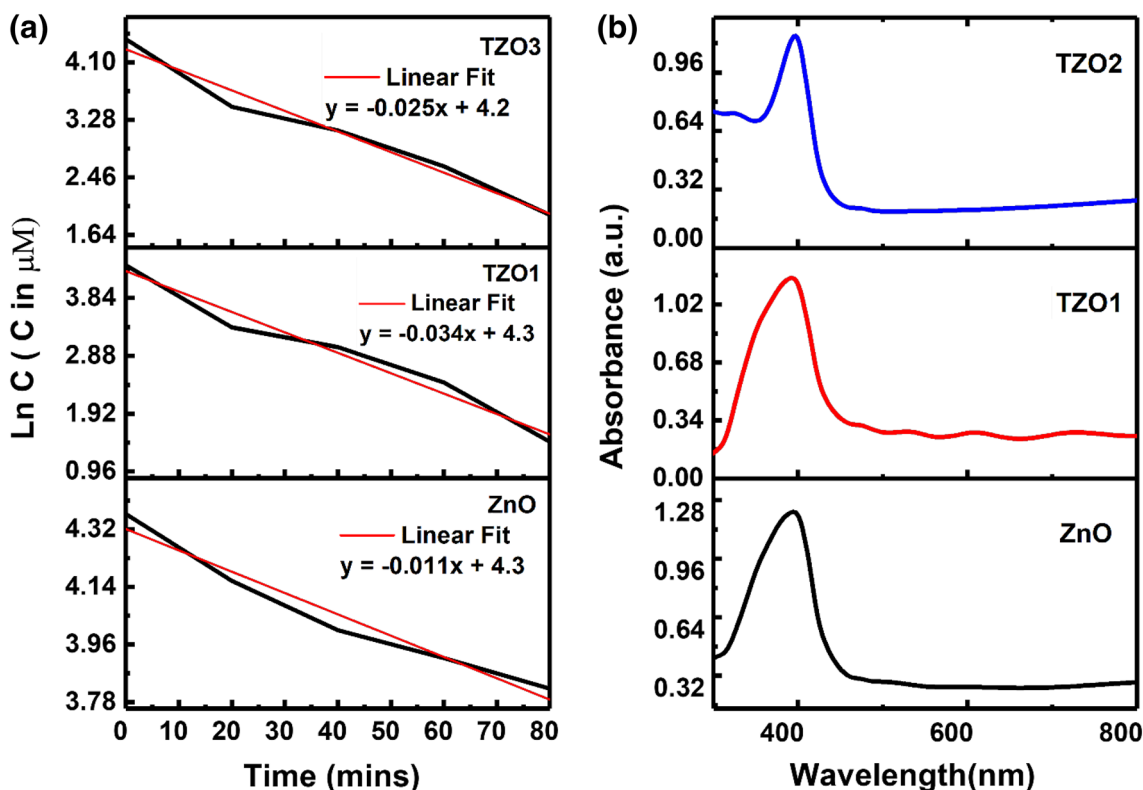
Fig. 10 a Plot showing the linear regression curve fit for the natural logarithm of absorbance of the methylene blue concentration against irradiation time for ZnO, TZO1 and TZO2. The TZO1 sample exhibits superior photocatalytic activity compared to ZnO and TZO2 sam-ples. **b** Absorbance spectrum of ZnO, TZO1 and TZO2. ZnO nanoparticles show maximum absorbance at 392 nm corresponding to a band gap of 3.22 eV which is redshifted to a band gap of 3.16 eV in the case of TZO1

parameters for various optoelectronic applications and in integrated optical devices (switches, modulators, filters, etc.). The extraction coefficient is defined as the fraction of energy which is lost due to scattering and absorption per unit thickness in a particular medium and it was calculated from Eq. (16) shown below [63]:

$$k = a\lambda/4\pi \tag{16}$$

The spectral dependence of k in the visible region is shown in Fig. 14a. The small values of k obtained in the visible region of the spectrum indicated a high transparency of the prepared thin films. In the case of the TZO2 film, a small increase in the k value at a higher wavelength indicated that the excess Sn segregated to the grain boundaries acted as scattering centers, which corroborated with XRD data as extinction coefficient is directly related to the creation of defects and absorption centers. The refractive index was calculated from the following equation [63]:

$$n = (1 + R/1 - R) + [4R/(R - 1)^2 - k^2]^{1/2} \tag{17}$$

where R is the reflectance and k is the extinction coefficient.

The variation of the refractive index of ZnO and TZO1 with wavelength is shown in Fig. 14b. It is clear that a sharp

increase in refractive index was observed near its optical absorption edge and then decreased as the wavelength increased. This is due to the increase in transmissivity and decrease in absorption coefficient in the visible region of spectrum. The decrease in refractive index observed in TZO1 as compared to ZnO is attributed to an increase in the carrier density of the film as variations in refractive index is mainly because of the interactions between photons and electrons in the films [64].

4.6.4 Photocurrent properties

The photocurrent characteristics of the prepared film is shown in Fig. 15. Only the prepared TZO1 thin film showed an enhanced increase in current response when irradiated with UV light. An increase in photocurrent is due to the photo excitation of electrons from VB into CB. When the films are irradiated with UV light, photon energy is absorbed and since the photon energy of UV light is higher than the optical band gap energy of the films, phot-generated charge carriers are created [65]. The magnitude of photocurrent obtained was higher at all bias voltages for TZO1 as compared to the I–V spectra for the TZO1 film which was
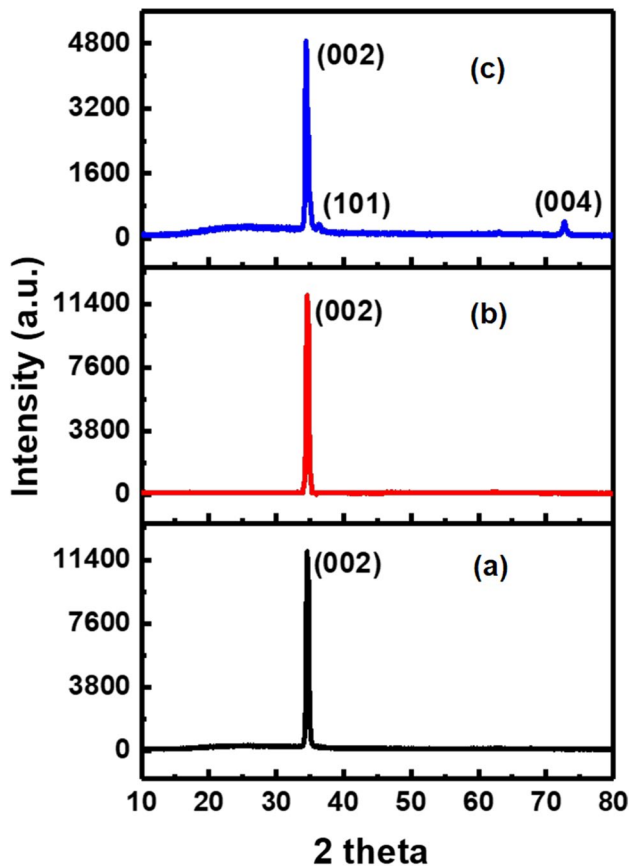
Fig. 11 XRD diffraction patterns of thin films **a** ZnO, **b** TZO1 and **c** TZO2. Sharp and strong (002) peak corresponds to the hexagonal wurtzite of ZnO. The decrease in intensity at the (002) plane for the TZO2 film indicates that the crystalline quality of thin film is deteriorated at higher doping amount

Fig. 12 Current–Voltage characteristics of films **a** ZnO, **b** TZO1 and **c** TZO2. The lowest resistivity of 1.4×10^{-3} Ωcm is obtained with 5% Sn in TZO1 film and the highest resistivity of 8.2×10^{-3} Ωcm is obtained with undoped ZnO film. Linear fit overlaps with the I–V curves

obtained without UV illumination. The I–V spectra obtained for the ZnO and TZO2 films with and without UV illumination exhibited no significant changes in the photocurrent values. The photocurrent properties of AZO films were investigated by Mammat et al. [65] by varying doping amounts of Al with and without UV light illumination. It was observed that higher magnitude of photocurrent was obtained with 1% Al doping amount and lower photocurrent values were observed with undoped ZnO film. In our study also, the ZnO thin film exhibited an insignificant rise in photocurrent due to its low carrier density and with TZO2 film, the
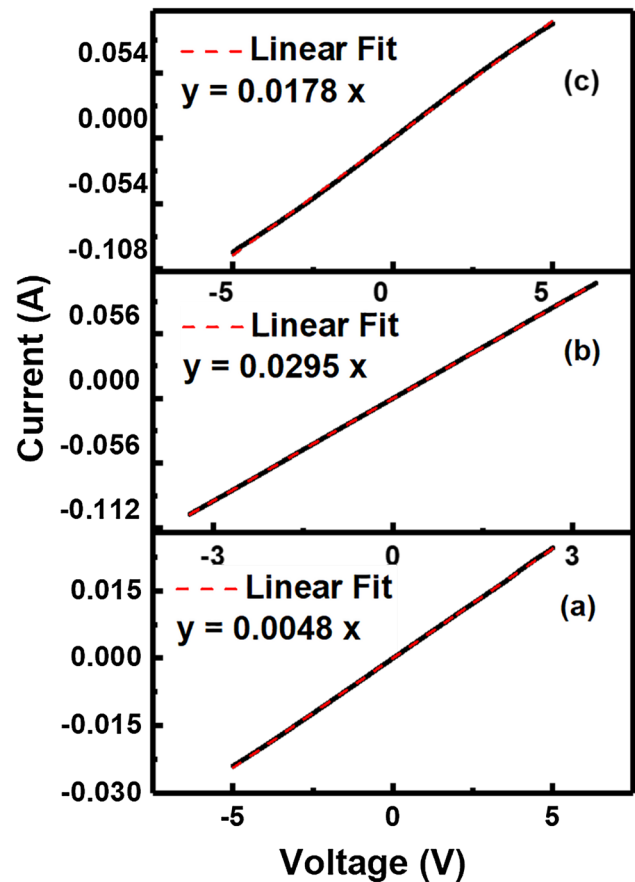
low mobility value and more defects arising out of excess Sn affected its photocurrent properties.

5 Figure of merit

For applications as transparent contacts, a film must have a low resistivity and high transmissivity in the region of visible spectrum. The figure of merit as defined by Haacke [66] is calculated as the criterion to determine the performance of transparent conducting oxides, as follows:

$$FOM = T^{10}/Rs \tag{18}$$

Table 2 The electrical properties of ZnO and TZO films

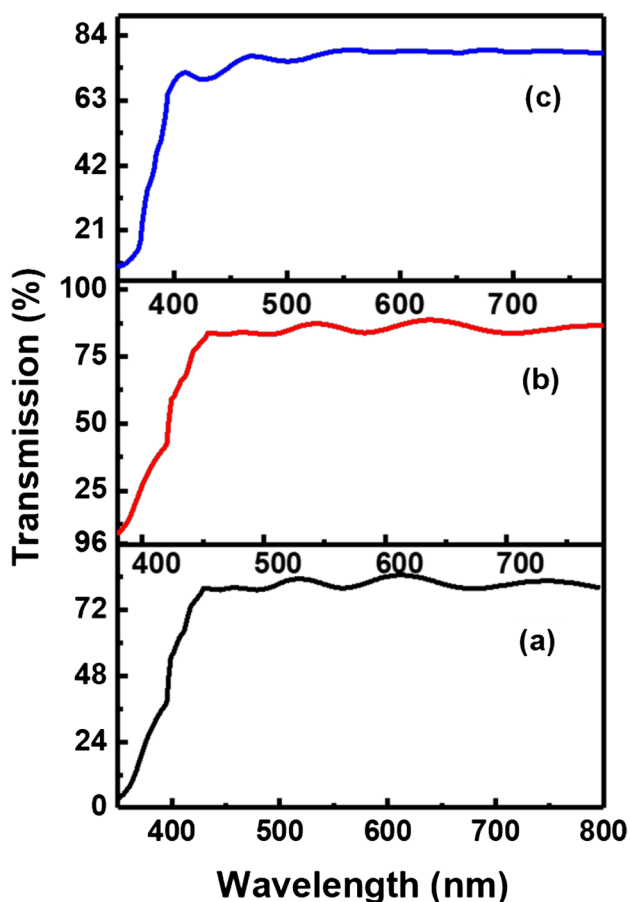| Magnetc field	Type of film	Carrier density (cm^3)	Resistivity (Ωcm)	Mobility (cm^2/V s)
0.35	ZnO	6.6×10^{19}	8.2×10^{-3}	11.6
0.35	TZO1	7.6×10^{19}	1.4×10^{-3}	58.7
0.35	TZO2	1.8×10^{20}	2.3×10^{-3}	15.1

Fig. 13 Plot of transmission curves versus wavelength for **a** ZnO, **b** TZO1 and **c** TZO2. All films exhibit an average transmittance of 80%

where T is the average transmittivity in the visible region and Rs is the sheet resistance. As shown in Table 3, the highest figure of merit 3.2×10^{-3} is obtained for TZO1. High FOM values imply that the prepared films are suitable in various optoelectronic applications.

6 Conclusions

Plasma-assisted chemical vapor synthesis carried out has shown a tremendous potential as a technique to synthesize nano-sized powders. Large-scale production of nanoparticles can be achieved due to the availability of high processing temperature to rapidly volatize reactants completely and rapidly, versatility of wide choice of reactants and a high quench rate to form nanosized particles. Results from XRD revealed that the doped and undoped ZnO nanopowders are purely crystalline and belong to the hexagonal wurtzite structure of ZnO. The presence of tin oxide peaks in TZO2 indicates that the Sn content has exceeded the maximum solubility in ZnO. The TZO1 (3 at.% Sn) nano powder exhibited a higher photocatalytic activity than ZnO in the degradation of methylene blue due to increased specific surface area and higher oxygen vacancies. The deposited films exhibited excellent electric properties and obtained resistivity was in the order of 10^{-3} Ωcm, TZO1 showed the highest carrier density of 7.6×10^{19} cm^{-3} and lowest electrical resistivity of 1.4×10^{-3} Ωcm of all films. Optical transmission approached 80% in the visible range for all

Fig. 14 **a** Plot of extinction coefficient versus wavelength for ZnO, TZO1 and TZO2. The small values of k obtained in the visible region of the spectrum indicate the high transparency of the prepared thin films. **b** The variation of refractive index with wavelength ZnO and TZO1. The decrease in refractive index is observed in TZO1 as compared to ZnO is due to an increase in the carrier concentration of the film
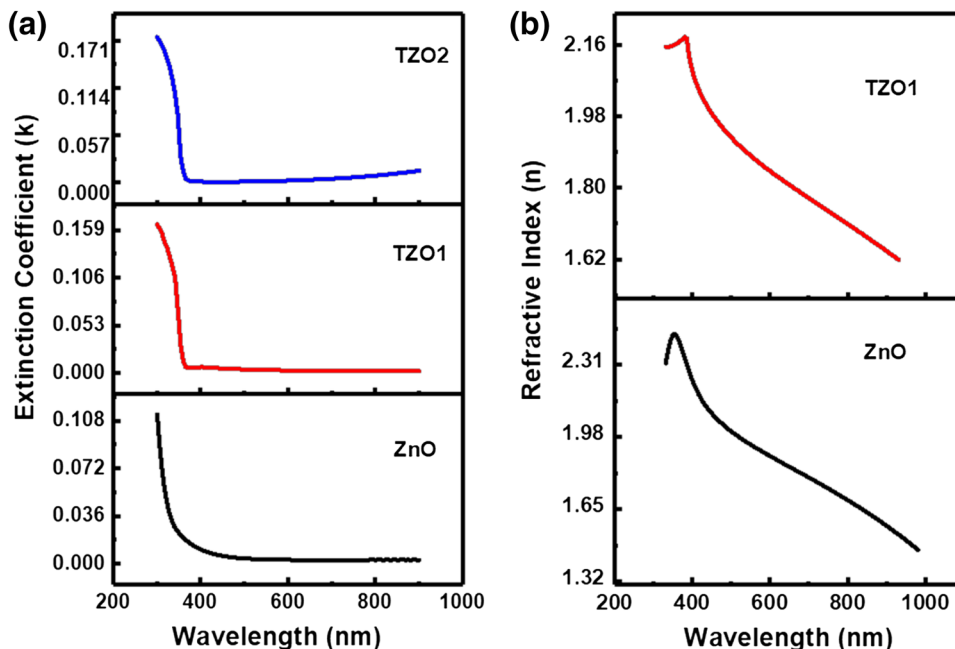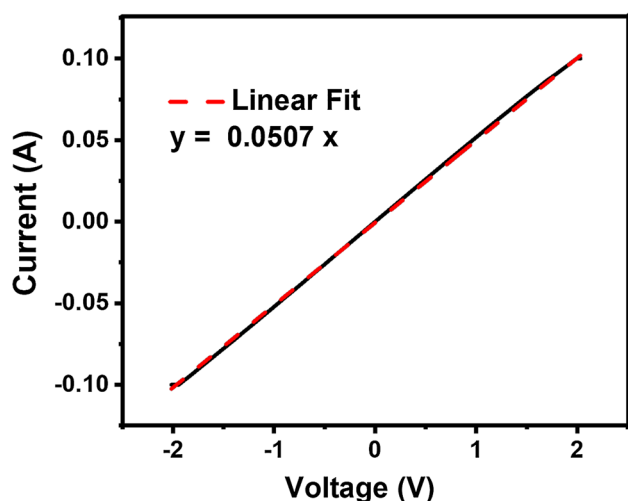
Fig. 15 Current–Voltage characteristic curve of TZO1 film under UV light illumination. An increase in photocurrent values at all bias voltages for TZO1 was obtained as compared to the I–V spectra for the TZO1 film obtained without UV illumination. Linear fit overlaps with the I–V curve

Table 3 Figure of merit values for ZnO and TZO films

Type	T^{10}/Rs (Ω^{-1})
ZnO	5.2×10^{-4}
TZO1	3.2×10^{-3}
TZO2	1.9×10^{-3}

deposited films, thus making it suitable for optoelectronic applications.

References

1. D.S.Y. Jayathilake, T.A.N. Peiris, J.S. Sagu, D.B. Potter, K.G.U. Wijayantha, C.J. Carmalt, D.J. Southee, ACS Sustain. Chem. Eng. **5**, 4820 (2017)
2. T. Shiosaki, M. Adachi, A. Kawabata, Thin Solid Films **96**, 129 (1982)
3. C.-T. Chen, F.-C. Hsu, Y.-M. Sung, H.-C. Liao, W.-C. Yen, W.-F. Su, Y.-F. Chen, Sol. Energy Mater. Sol. Cells **107**, 69 (2012)
4. S. Xue, X. Zu, W. Zheng, M. Chen, X. Xiang, Phys. B **382**, 201 (2006)
5. C. Benouis, M. Benhaliliba, A.S. Juarez, M. Aida, F. Chami, F. Yakuphanoglu, J. Alloys Compd. **490**, 62 (2010)
6. T.T. Werner, G.M. Mudd, S.M. Jowitt, Appl. Earth Sci. **124**, 213 (2015)
7. R. Deng, X. Zhang, J. Lumin. **128**, 1442 (2008)
8. M. Tsega, D.-H. Kuo, Solid State Commun. **164**, 42 (2013)
9. J.-H. Lee, B.-O. Park, Thin Solid Films **426**, 94 (2003)
10. Z. Heinrich, *Color Chemistry: Synthesis, Properties and Applications of Organic Dyes and Pigments* (Wiley-VCH, Weinheim, 2003)
11. A.G. Prado, J.D. Torres, E.A. Faria, S.Ä.Ì.C. Dias, J. Colloid Interface Sci. **277**, 43 (2004)
12. S. Senthilvelan, V. Chandraboss, B. Karthikeyan, L. Natanapatham, M. Murugavelu, Mater. Sci. Semicond. Process. **16**, 185 (2013)
13. M. Huang, C. Xu, Z. Wu, Y. Huang, J. Lin, J. Wu, Dyes Pigm. **77**, 327 (2008)
14. J. Jing, J. Li, J. Feng, W. Li, W.W. Yu, Chem. Eng. J. **219**, 355 (2013)
15. K.M. Reza, A. Kurny, F. Gulshan, Appl. Water Sci. **7**, 1569 (2015)
16. A. Gnanaprakasam, V.M. Sivakumar, M. Thirumarimurugan, Indian J. Mater. Sci. **2015**, 1 (2015)
17. H.Y. Sohn, *Chemical Vapor Synthesis of Inorganic Nanopowders* (Nova Science Publishers, New York, 2012)
18. A. Murali, H.Y. Sohn, Mater. Res. Express **5**, 065045 (2018)
19. C.U. Bang, D.H. Shin, Y.C. Hong, H.S. Uhm, IEEE Conference Record—Abstracts. 2005 IEEE International Conference on Plasma Science (2005)
20. G. Buhler, D. Tholmann, C. Feldmann, Adv. Mater. **19**, 2224 (2007)
21. J. Ederth, P. Heszler, A. Hultaker, G. Niklasson, C. Granqvist, Thin Solid Films **445**, 199 (2003)
22. C. Wu, L. Shen, H. Yu, Q. Huang, Y.C. Zhang, Mater. Res. Bull. **46**, 1107 (2011)
23. L.-P. Wang, F. Zhang, S. Chen, Z.-H. Bai, Int. J. Mine. Metall. Mater. **24**, 455 (2017)
24. M.A. Javid, M. Rafi, I. Ali, F. Hussain, M. Imran, A. Nasir, Mater. Sci. **34**, 741–746 (2016)
25. P. Junlabhut, W. Mekprasart, R. Noonuruk, K. Chongsri, W. Pecharapa, Energy Procedia **56**, 560 (2014)
26. M. Verma, P.K. Dwivedi, B. Das, J. Exp. Nanosci. **10**, 438 (2013)
27. S.Y. Li, P. Lin, C.Y. Lee, T.Y. Tseng, C.J. Huang, J. Phys. D **37**, 2274 (2004)
28. V. Shelke, B.K. Sonawane, M.P. Bhole, D.S. Patil, J. Mater. Sci.: Mater. Electron. **23**, 451 (2011)
29. F. Bedia, A. Bedia, M. Aillerie, N. Maloufi, B. Benyoucef, Energy Procedia **74**, 539 (2015)
30. M. Nasir, M. Hannas, M.H. Mamat, M. Rusop, Adv. Mater. Res. **1109**, 577 (2015)
31. T. Ryu, Y.J. Choi, S. Hwang, H.Y. Sohn, I. Kim, J. Am. Ceram. Soc. **93**, 3130 (2010)
32. B. Liu, X. Zhao, C. Terashima, A. Fujishima, K. Nakata, Phys. Chem. Chem. Phys. **16**, 8751 (2014)
33. . D. Cullity, *Elements of X-Ray Diffraction* (Addison-Wesley Publishing Company, Reading, 1967)
34. O. Lupan, S. Shishiyanu, V. Ursaki, H. Khallaf, L. Chow, T. Shishiyanu, V. Sontea, E. Monaico, S. Railean, Sol. Energy Mater. Sol. Cells **93**, 1417 (2009)
35. A. Drici, G. Djeteli, G. Tchangbedji, H. Derouiche, K. Jondo, K. Napo, J.C. Bernede, S. Ouro-Djobo, M. Gbagba, Phys. Status Solidi A **201**, 1528 (2004)
36. T.C. Damen, S.P.S. Porto, B. Tell, Phys. Rev. **142**, 570 (1966)
37. J. Alaria, M. Bouloudenine, G. Schmerber, S. Colis, A. Dinia, P. Turek, M. Bernard, J. Appl. Phys. **99**, 08M118 (2006)
38. S. Hamrit, K. Djessas, N. Brihi, B. Viallet, K. Medjnoun, S. Grillo, Ceram. Int. **42**, 16212 (2016)
39. P. Sangeetha, V. Sasirekha, V. Ramakrishnan, J. Raman Spectrosc. **42**, 1634 (2011)
40. H. Liu, X. Zeng, X. Kong, S. Bian, J. Chen, Appl. Surf. Sci. **258**, 8564 (2012)
41. D. Choi, Y.S. Kim, Y. Son, RSC Adv. **4**, 50975 (2014)
42. K.J. Chen, F.Y. Hung, Y.T. Chen, S.J. Chang, Z.S. Hu, Mater. Trans. **51**, 1340 (2010)

43. A. Bougrine, A.E. Hichou, M. Addou, J. Ebothe, A. Kachouane, M. Troyon, Mater. Chem. Phys. **80**, 438 (2003)
44. M. Gao, X. Wu, J. Liu, W. Liu, Appl.Surf. Sci. **257**, 6919 (2011)
45. B.-Y. Oh, M.-C. Jeong, J.-M. Myoung, App. Surf. Sci. **253**, 7157 (2007)
46. X.-J. Yang, X.-Y. Miao, X.-L. Xu, C.-M. Xu, J. Xu, H.-T. Liu, Opt. Mater. **27**, 1602 (2005)
47. C.-A. Tseng, J.-C. Lin, W.-H. Weng, C.-C. Lin, Jpn. J. Appl. Phys. **52**, 025801 (2013)
48. P.-T. Hsieh, Y.-C. Chen, K.-S. Kao, C.-M. Wang, Appl, Phys. A **90**, 317 (2007)
49. P. Zu, Z.K. Tang, G.K. Wong, M. Kawasaki, A. Ohtomo, H. Koinuma, Y. Segawa, Solid State Commun. **103**, 459 (1997)
50. S.-S. Lo, D. Huang, C.H. Tu, C.-H. Hou, C.-C. Chen, J. Phys. D **42**, 095420 (2009)
51. Y.J. Jang, C. Simer, T. Ohm, Mater. Res. Bull. **41**, 67 (2006)
52. T.N. Ravishankar, K. Manjunatha, T. Ramakrishnappa, G. Nagaraju, D. Kumar, S. Sarakar, B. Anandakumar, G. Chandrappa, V. Reddy, J. Dupont, Mater. Sci. Semicond. Process. **26**, 7 (2014)
53. B.M. Rajbongshi, A. Ramchiary, S.K. Samdarshi, Mater. Lett. **134**, 11 (2014)
54. M. Khairy, W. Zakaria, Egypt. J. Pet. **23**, 419 (2014)
55. S.A. Ansari, M.M. Khan, J. Lee, M.H. Cho, J. Ind. Eng. Chem. **20**, 1602 (2014)
56. C. Wang, D. Wu, P. Wang, Y. Ao, J. Hou, J. Qian, App. Surf. Sci. **325**, 112 (2015)
57. B. Choudhury, P. Chetri, A. Choudhury, RSC Adv. **4**, 4663 (2014)
58. A. Younis, D. Chu, Y.V. Kaneti, S. Li, Nanoscale **8**, 378 (2016)
59. J. Shao, Y.Q. Shen, J. Sun, N. Xu, D. Yu, Y.F. Lu, J.D. Wu, J. Vac. Sci. Technol. B **26**, 214 (2008)
60. W. Yang, Z. Liu, D.-L. Peng, F. Zhang, H. Huang, Y. Xie, Z. Wu, Appl. Surf. Sci. **255**, 5669 (2009)
61. A. Sreedhar, J.H. Kwon, J. Yi, J.S. Gwag, Mater. Res. Bull. **95**, 451 (2017)
62. C.-Y. Tsay, H.-C. Cheng, Y.-T. Tung, W.-H. Tuan, C.-K. Lin, Thin Solid Films **517**, 1032 (2008)
63. F. Abeles, *Optical Properties of Solids* (North-Holland, Amsterdam, 1972)
64. M. Caglar, S. Ilican, Y. Caglar, F. Yakuphanoglu, J. Mater. Sci.: Mater. Electron. **19**, 704 (2007)
65. M.H. Mamat, M.Z. Sahdan, Z. Khusaimi, A.Z. Ahmed, S. Abdullah, M. Rusop, Opt. Mater. **32**, 696 (2010)
66. G. Haacke, J. Appl. Phys. **47**, 4086 (1976)